Stability and local electronic properties of Al_3M (M=Zr,Hf): An NMR study

C. S. Lue,* B. X. Xie, S. N. Horng, J. H. Su, and J. Y. Lin
Department of Physics, National Cheng Kung University, Tainan 70101, Taiwan
(Received 2 January 2005; published 9 May 2005)

^{27}Al NMR measurements were performed on the $D0_{23}$-structure trialuminides Al_3Zr and Al_3Hf. The Knight shifts, quadrupole splittings, and spin-lattice relaxation times for each of the three crystallographic sites have been resolved. Universally small Fermi-contact Knight shifts and long relaxation times are found for both alloys. Results provide a measure of *s*-character Fermi-level density of states $N_s(E_F)$ and an indication of orbital weights. In addition, there is evidence that $N_s(E_F)$ correlates with the structural stability of the studied materials. Our NMR measurements confirm that Al_3Zr is more stable than Al_3Hf with respect to the $D0_{23}$ structure.

DOI: 10.1103/PhysRevB.71.195104 PACS number(s): 76.60.−k, 71.20.Be

I. INTRODUCTION

Transition-metal-based trialuminides (Al_3M) exhibit a unique combination of properties such as high melting points, low mass densities, and low oxidation resistances. A great deal of research has been devoted to investigating these materials for the understanding of their electronic properties and structural phase stability.[1–8] Among these Al_3M alloys (where M is the early transition element Ti, V, Zr, Nb, Hf, …), the possible crystal structures are $L1_2$ and $D0_{22}$, as well as $D0_{23}$.[9] For Al_3Zr and Al_3Hf, the low-temperature ground state $D0_{23}$ is energetically favored, while Al_3Hf is more stable with $D0_{22}$ at high temperatures.[10]

Theoretically, electronic-structure calculations performed simply by optimizing the c/a ratio could not predict a correct ground state for both alloys.[11–13] On the other hand, allowing the internal atoms shifting off their ideal positions is a key source responsible for the $D0_{23}$-structure stability.[14–17] The calculated total density of states (DOS) exhibited a deep valley at the Fermi level, attributed to hybridization between Al *p* and *M d* playing an important role for the DOS reduction. Nevertheless, there has been little experimental work associated with these scenarios, essential to interpret their structural stability.

As shown in Fig. 1, the crystal structure of $D0_{23}$ is a superstructure which consists of a stacking of four $L1_2$ cubes with the same antiphase shifts every two cubes. There are three nonequivalent Al sites with equal population, denoted as Al-I, Al-II, and Al-III, respectively. Al-I, interacting with four transition atoms in the (100) plane, has point symmetry *mmm* which is nonaxial with respect to the *c* axis. Al-II, with point symmetry $\bar{4}m2$, is surrounded by two transition elements in the (100) and two in the (010) planes. The atomic position of Al-III, located in the (001) plane with four first-nearest transition element neighbors, is not fixed in the *c* direction due to its 4*mm* symmetry. The (100), (010), and (001) planes are not equivalent due to noncubic symmetry. With the study of interactions between transition atoms and individual Al sites, the results can be utilized to examine the local electronic properties of $D0_{23}$. Nuclear magnetic resonance (NMR) is known as an atomic probe in metallic alloys yielding information on site occupation and Fermi surface features. In this paper, we will present NMR measurements including the Knight shifts, quadrupole transitions, and spin-lattice relaxation times in Al_3Zr and Al_3Hf as related to their local electronic characteristics. The information about the local environments is mainly obtained through the quadrupole interactions as well as through the hyperfine interactions in this investigation.

II. EXPERIMENT AND DISCUSSION

The polycrystalline compounds were prepared by an ordinary arc-melting technique. Briefly, a mixture of appropriate amounts of high-purity elemental metals was placed in a water-cooled copper hearth and then melted several times in an argon-flow arc melter. The weight loss during melting is less than 0.05% for each compound. To promote homogeneity, both materials were annealed in a vacuum-sealed quartz tube at 900 °C for 7 days, followed by furnace cooling. This process is not trivial because metastable phases may appear in these materials as the annealing temperature is below 500 °C.[18,19] The resulting ingots, which tend to be brittle, were grounded to powder. A room-temperature x-ray diffraction taken with Cu $K\alpha$ radiation on powder samples is shown in Fig. 2. Strong reflections in both alloys could be indexed

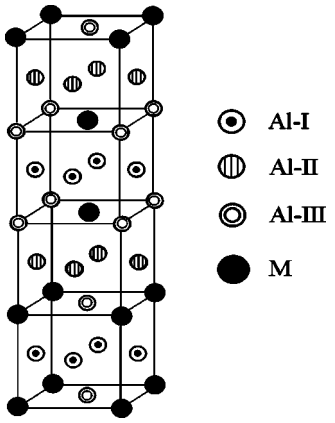

FIG. 1. Crystal structure for the $D0_{23}$-type trialuminide intermetallics.

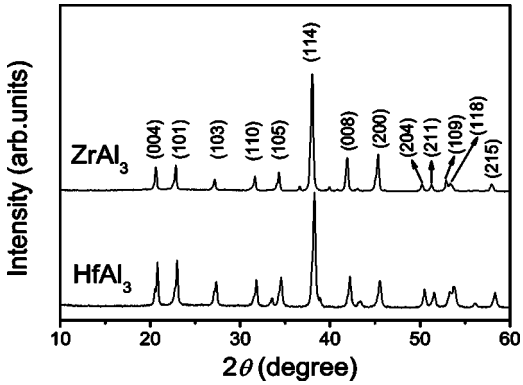

FIG. 2. X-ray diffraction patterns in Al_3Zr and Al_3Hf. Reflections are indexed with respect to the $D0_{23}$ structure.

according to the expected $D0_{23}$ structure. Several weak peaks remain unidentified which had little effect on the NMR measurements. A more detailed analysis of the x-ray data, in which the $D0_{23}$ structure was refined with the Rietveld method, was conducted. We thus obtained the lattice constants $a=0.4005$ nm and $c=1.7261$ nm for Al_3Zr, and $a=0.3985$ nm and $c=1.7136$ nm for Al_3Hf. These values were found to be close to those reported in the literature.[14,20,21]

NMR measurements were performed using a Varian 300 spectrometer, with a constant field of 7.05 T. A homebuilt probe was employed for both room-temperature and high-temperature experiments. Since the studied materials are metals, powder samples were used to avoid the skin depth problem of the rf transmission power. Each specimen was put in a plastic vial that showed no observable ^{27}Al NMR signal. The Knight shifts here were referred to the ^{27}Al resonance frequency of one molar aqueous $AlCl_3$.

A. Line shape and isotropic Knight shift

Central transition $\left(m=\frac{1}{2}\leftrightarrow-\frac{1}{2}\right)$ line shapes were obtained from spin-echo fast Fourier transforms using a standard

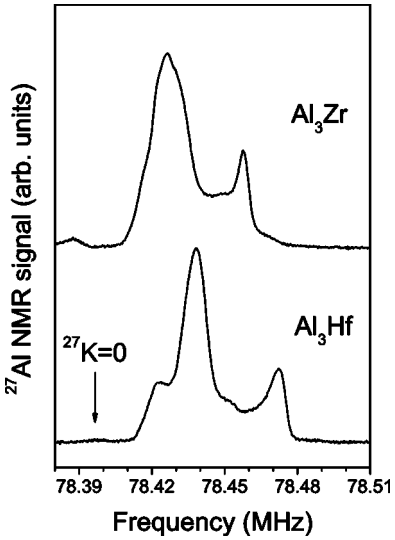

FIG. 3. ^{27}Al central transition NMR spectra for Al_3Zr and Al_3Hf measured at room temperature. The arrow indicates the ^{27}Al zero Knight shift.

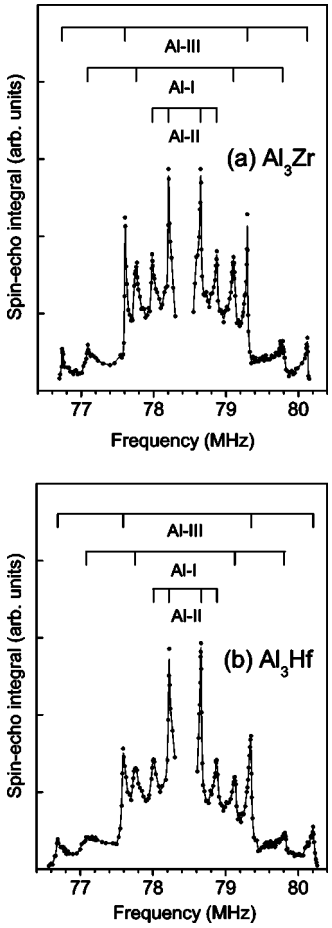

FIG. 4. Fully resolved satellite line shapes for the three Al sites in Al_3Zr and Al_3Hf.

$\pi/2$-τ-π sequence. Since powder materials were used in our NMR experiment, the central transition lines appear as powder patterns, as given in Fig. 3. The spectrum is quite complicated because of the combination of three Al sites and the simultaneous presence of anisotropic Knight shift and second-order quadrupole effects. Attempts to decompose the spectrum into three component lines using quadrupolar broadening together with anisotropic Knight cannot yield an unambiguous result. On the other hand, we can measure the isotropic Knight shift K_{iso} of each site by taking the midpoint of the separated satellite pairs [shown in Figs. 4(a) and 4(b)]. The obtained K_{iso} values were tabulated in Table I. For Al_3Zr, the corresponding shifts are close to those obtained by using the magic-angle spinning technique,[22] suggesting a reasonable estimate presented here. Also our Knight shift analysis reveals that the high-frequency peak is mainly dominated by site III, while the low-frequency part is a mixture of sites I and II.

From the relationship of the isotropic Knight shift to the *s*-DOS in metals,[23] the small K_{iso} for both compounds implies low DOS at the Fermi surfaces. In addition, the larger K_{iso} occurring at site III indicates more *s* electrons at this site. However, K_{iso} is not entirely due to the *s*-contact Knight shift (K_s) because the *s*-*d* mixing (K_{sd}) and orbital shift (K_{orb}) also contribute to K_{iso}. Although those terms are usually much smaller than the *s*-contact Knight shift in paramag-

TABLE I. Asymmetry parameter, quadrupole frequency, isotropic Knight shift, Fermi-contact Knight shift, exchange polarization and orbital Knight shifts, and room-temperature spin-lattice relaxation time for each of the Al site.

Alloy	Site	η	ν_Q (MHz)	K_{iso} (%)	K_s (%)	$K_{sd}+K_{orb}$ (%)	T_1 (ms)
Al_3Zr	I	0.028	1.345	0.046	0.016	0.030	125±4
	II	0	0.445	0.043	0.016	0.027	126±7
	III	0	1.690	0.069	0.025	0.044	54±8
Al_3Hf	I	0.027	1.375	0.053	0.016	0.037	127±9
	II	0	0.440	0.060	0.026	0.034	50±4
	III	0	1.760	0.094	0.033	0.061	29±3

netic metals, they become competitive when the latter is significantly small.

According to the noninteracting electron picture, the *s*-contact Knight shift can be expressed as $K_s = \mu_B H_{hf}^s N_s(E_F)$. Here μ_B is the Bohr magneton, H_{hf}^s is the hyperfine field of the *s* electrons, and $N_s(E_F)$ is the *s*-DOS at the Fermi level. With the estimate of $H_{hf}^s \sim 1.9\times10^6$ G in Al metal[24] and $N_s(E_F)$ deduced from T_1 measurements as mentioned later, K_s was thus obtained with the results shown in Table I. Universally small Fermi-contact Knight shifts are extracted for all Al sites in both Al_3Zr and Al_3Hf. While we cannot distinguish K_{sd} and K_{orb} in the present study, the exchange polarization of *s* electrons by *d* states generally contributes to a negative shift due to the negative hyperfine field of *d* electrons.[25,26] This implies that the observed shifts are mainly associated with the orbital term, especially for Al site III.

B. Quadrupole interaction and electric field gradient

In order to explore the local electronic properties for each Al site, we performed quadrupole transition measurements providing well-resolved satellite lines for individual sites. In this investigation, wide-line satellite spectra were mapped out by integrating spin-echo signals of various excitations. Due to electric quadrupole coupling, the ^{27}Al NMR spectra $\left(I=\frac{5}{2}\right)$ are composed of 5 transition lines per site, so that 3 nonequivalent Al sites in $D0_{23}$ result in 15 lines, as demonstrated in Fig. 4 (three central transition lines have been displayed separately in Fig. 3). For powdered samples, as in our experiment, these lines exhibit as typical powder patterns, with distinctive edge structures corresponding to the quadrupole parameters. The four edge singularities for each Al site correspond to $m=\pm\frac{1}{2}\leftrightarrow\pm\frac{3}{2}$ and $m=\pm\frac{3}{2}\leftrightarrow\pm\frac{5}{2}$ transitions. Since the first-order quadrupole shift is the main effect shaping the satellite line, the quadrupole frequency ν_Q was determined directly from these lines. Due to the axial symmetry for Al-II and Al-III, the ν_Q values can be obtained from the difference between $m=-\frac{1}{2}\leftrightarrow-\frac{3}{2}$ and $m=+\frac{1}{2}\leftrightarrow+\frac{3}{2}$ edges. Site identification for the Al_3Zr alloy has been given by Bastow *et al.*[22] Accordingly, the smaller ν_Q has been assigned to site II and the larger one to site III. For Al-I, however, the point symmetry (*mmm*) is nonaxial which yields a nonzero asymmetry parameter $\eta=|(V_{yy}-V_{xx})/V_{zz}|$. Such an asymmetry effect splits the $m=\pm\frac{1}{2}\leftrightarrow\pm\frac{3}{2}$ transitions into two edges at $(1-\eta)\nu_Q/2$ and $(1+\eta)\nu_Q/2$, as demonstrated in Fig. 5. We can thus determine ν_Q using the central position of these lines and the η factor from the observed splitting for this site. All extracted ν_Q and η values for Al_3Zr and Al_3Hf were summarized in Table I. It is interesting that the differences in ν_Q and η between the compounds are marginal, indicative of the similar local charge environments within both alloys.

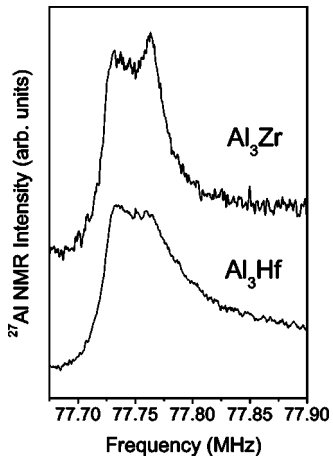

FIG. 5. Quadrupole transitions of $m=-\frac{1}{2}\leftrightarrow-\frac{3}{2}$ for the Al site I of Al_3Zr and Al_3Hf.

From ν_Q for each Al site, we can determine the electric field gradient (EFG). Here $\nu_Q=3eQV_{zz}/(2I(2I-1)h$ is defined by the nuclear quadrupole moment Q and the largest principal-axis component of the EFG tensor V_{zz}. This effect arises from the noncubic arrangement of the charged lattice ions and the nonuniform charge density of the conduction electrons due to orbital motion. Attempts to reproduce the observed EFG's with a simple point-charge model yield unreasonable charge transfers. In fact, the electronegativity difference between transition-metal and Al atoms is low and hence the ionicity does not play a significant role in the bonding nature of the studied compounds. On this basis, the valance charges would be the major source for the observed EFG's. Since the largest ν_Q consistently appears at site III, we attributed the large EFG to the concentration of bonding charges in the *ab* planes. This confirms the importance of *p-d* hybridization between Al site III and the transition metal for the structural properties of these materials.

C. Spin-lattice relaxation time and Fermi-level density of states

As seen from Fig. 3, three Al NMR lines are strongly mixed, leading to the difficulty of the separation of individual sites from the central transition signals. We thus measured the spin-lattice relaxation time (T_1) using the satellite lines, providing distinctive peaks for each Al site. We found each T_1 by centering the transmission frequency at the $m=-\frac{1}{2}\leftrightarrow-\frac{3}{2}$ quadrupole-split powder pattern edges, where the resonance is dominated by one site. The spin-lattice relaxation time measurements were carried out using the inver-

sion recovery method. We recorded the signal strength by integrating the recovered spin-echo signal. In these experiments, the relaxation process involves the adjacent pairs of spin levels, and the corresponding spin-lattice relaxation is a multiexponential expression.[27] For the $m=-\frac{1}{2}\leftrightarrow-\frac{3}{2}$ transition with $I=\frac{5}{2}$, the recovery of the nuclear magnetization M follows

$$\frac{M(t)-M(0)}{M(0)} = -2(0.157e^{-t/T_1}+0.054e^{-3t/T_1}+0.075e^{-6t/T_1} + 0.446e^{-10t/T_1}+0.268e^{-15t/T_1}), \quad (1)$$

derived from the initial conditions used in our experiments. Here $M(0)$ is the initial magnetization after inversion and $M(t)$ is the magnetization at the recovery time t. Thus T_1 values can be obtained by fitting to this multiexponential recovery curve. To provide accurate values, each T_1 has been measured several times and the averaged T_1 for each Al site is enumerated in Table I. While nonconduction mechanisms may contribute to the relaxation, they were excluded by the Korringa relation.[28] T_1 measurements performed at various temperatures yield Korringa behavior (constant T_1T), indicating a conduction-electron mechanism for the observed relaxation. In addition, no exotic behavior in $1/T_1$ at high temperatures suggests that Al_3Zr and Al_3Hf are better classified as metals instead of semimetals like Fe_2VAl.[29,30]

The spin-lattice relaxation time measurement is known as a direct probe of the Fermi surface feature in nonmagnetic materials. For the present Al_3Zr and Al_3Hf, the relaxation of Al nuclei is dominated by their coupling to the spin of the *s*-character electrons. In the absence of collective electron effects, the relaxation rate is simply governed by the initially occupied and finally unoccupied electronic states, associated with the hyperfine field arising from contact electrons. Under such an approximation, the spin-lattice relaxation rate can be written as[31]

$$\frac{1}{T_1} = 2hk_BT[\gamma_n H_{hf}^s N_s(E_F)]^2, \quad (2)$$

where h, k_B, and T are the Planck constant, Boltzmann constant, and absolute temperature, respectively. γ_n is the Al nuclear gyromagnetic ratio, H_{hf}^s is the hyperfine field of the Al *s* electrons, and $N_s(E_F)$ represents the *s*-DOS at the Fermi level. As indicated from Table I, the deduced T_1's were found to be much longer than that of the Al metal which is about 6 ms at room temperature.[32] The strong enhancement of T_1 is related to DOS reduction at the Fermi level, which has been proposed to account for the $D0_{23}$ phase stability.

For the aluminum atom, the states around the Fermi surface are predominately *s* and *p* like, the mixture of *d* states being rather small. Since *p* and *d* hyperfine fields are generally an order of magnitude smaller than *s* hyperfine fields,[24] the main hyperfine field in such alloys arises from contact electrons. Taking $H_{hf}^s \sim 1.9\times10^6$ gauss in Al metal[24] and experimental T_1's, the Fermi level DOS of *s* electrons for each individual site can be obtained from Eq. (2), with the results listed in Table II. Higher *s*-DOS at the Fermi surface occurring at site III implies that more *s* electrons exist at that site, identical with the observation for site I in the $D0_{22}$ structure. Together with the EFG results, we conclude that Al-III in $D0_{23}$ plays a similar role for the local electronic properties and phase stability as Al-I in $D0_{22}$.[4]

TABLE II. Calculated Fermi level *s*-DOS (states/eV atom) for each Al crystallographic site, deduced from the NMR T_1's.

Alloy	Al-I	Al-II	Al-III	Total
Al_3Zr	0.0147	0.0146	0.0223	0.0172
Al_3Hf	0.0145	0.0232	0.0304	0.0227

From T_1 analysis, small Fermi-level densities of states were found for both studied alloys, in good agreement with theoretical predications of the presence of pseudogap near the Fermi level due to hybridizations.[14–16] Our high-temperature T_1 measurements further indicated that these hybridized pseudogaps are not as deep as those in semimetals. Moreover, we demonstrated that Al_3Zr contains less Al *s*-character Fermi-level DOS than that in Al_3Hf. The lower Fermi-level DOS is often related to the higher phase stability.[13] This can be understood as follows: If the Fermi-level DOS is small, it means that more electrons participate in bonding and get localized. As a result, the stability of the material will be larger. With this accordance, the present NMR study confirms that Al_3Zr is more stable than Al_3Hf with respect to the $D0_{23}$ structure. Such an argument is consistent with the fact that Al_3Hf becomes more favorable with $D0_{22}$ at high temperatures ($T>650$ °C).[10]

III. CONCLUSIONS

We have a concise picture of the NMR features for Al_3Zr and Al_3Hf, giving an experimental viewpoint for their local electronic properties. The Knight shifts together with relaxation times provide a measure of $N_s(E_F)$ and an indication of orbital weights. There is some evidence that $N_s(E_F)$ correlates with the stability for the $D0_{23}$ structure. We also have discussed the observed EFG's, which are consistent with a bonding configuration in the *ab* plane. A strong similarity was found for the NMR characteristics of both materials, pointing to a uniformity in the electronic-structure properties.

ACKNOWLEDGMENTS

We are grateful to Professor J. H. Ross, Jr. of Texas A&M University for early guidance on related projects. This work was supported by the National Science Council of Taiwan under Grant No. NSC-93-2112-M-006-001 (C.S.L.).

*Electronic address: cslue@mail.ncku.edu.tw

[1] J. H. Schneibel, P. F. Becher, and J. A. Horton, J. Mater. Res. **3**, 1272 (1988).
[2] M. Asta, D. de Fontaine, M. van Schilfgaarde, M. Sluiter, and M. Methfessel, Phys. Rev. B **46**, 5055 (1992).
[3] S. Liu, R. Hu, and C. Wang, J. Appl. Phys. **79**, 214 (1996).
[4] C.-S. Lue, S. Chepin, J. Chepin, and J. H. Ross, Jr., Phys. Rev. B **57**, 7010 (1998).
[5] L. Proville and A. Finel, Phys. Rev. B **64**, 054104 (2001).
[6] M. Krajči and J. Hafner, J. Phys.: Condens. Matter **14**, 1865 (2002).
[7] B. Fisher, K. B. Chashka, L. Patlagan, G. Bazalitsky, and G. M. Reisner, Phys. Rev. B **68**, 014118 (2003).
[8] C. L. Condron, G. J. Miller, J. D. Strand, S. L. Bud'ko, and P. C. Canfield, Inorg. Chem. **42**, 8371 (2003).
[9] W. B. Pearson, *A Handbook of Lattice Spacings and Structures of Materials and Alloys* (Pergamon, Oxford, 1967); *Binary Alloy Phase Diagrams*, 2nd ed., edited by T. B. Massalski, H. Okamoto, P. R. Subramanian, and L. Kacprzak (ASM International, Materials Park, OH, 1990).
[10] J. L. Murray, A. J. McAlister, and D. J. Kahan, J. Phase Equilib. **19**, 376 (1998).
[11] A. E. Carlsson and P. J. Meschter, J. Mater. Res. **4**, 1060 (1989).
[12] T. Hong, T. J. Watson-Yang, A. J. Freeman, T. Oguchi, and J. H. Xu, Phys. Rev. B **41**, 12462 (1990).
[13] J. H. Xu and A. J. Freeman, Phys. Rev. B **41**, 12553 (1990).
[14] C. Amador, J. J. Hoyt, B. C. Chakoumakos, and D. de Fontaine, Phys. Rev. Lett. **74**, 4955 (1995).
[15] C. Colinet and A. Pasturel, J. Alloys Compd. **319**, 154 (2001).
[16] C. Colinet and A. Pasturel, Phys. Rev. B **64**, 205102 (2001).
[17] E. Clouet, J. M. Sanchez, and C. Sigli, Phys. Rev. B **65**, 094105 (2002).
[18] S. Srinivasan, P. B. Desch, and R. B. Schwarz, Scr. Metall. Mater. **25**, 2513 (1991).
[19] J. Q. Guo and K. Ohtera, Mater. Lett. **27**, 343 (1996).
[20] J. C. Schuster and H. Nowotny, Z. Metallkd. **71**, 341 (1980).
[21] J. Maas, G. Bastin, F. Van Loo, and R. Metselaar, Z. Metallkd. **74**, 294 (1983).
[22] T. J. Bastow, C. T. Forwood, M. A. Gibson, and M. E. Smith, Phys. Rev. B **58**, 2988 (1998).
[23] C. P. Slichter, *Principles of Magnetic Resonance* (Springer-Verlag, New York, 1990).
[24] G. C. Carter, I. D. Weisman, L. H. Bennett, and R. E. Watson, Phys. Rev. B **5**, 3621 (1972).
[25] C.-S. Lue and J. H. Ross, Jr., Phys. Rev. B **60**, 8533 (1999).
[26] *Metallic Shifts in NMR*, edited by G. C. Carter, L. H. Bennett, and D. J. Kahan (Pergamon, Oxford, 1977).
[27] W. W. Simmons, W. J. O'Sullivan, and W. A. Robinson, Phys. Rev. **127**, 1168 (1962).
[28] J. Korringa, Physica (Amsterdam) **16**, 601 (1950).
[29] C. S. Lue and J. H. Ross, Jr., Phys. Rev. B **58**, 9763 (1998); **61**, 9863 (2000).
[30] C. S. Lue and Y.-K. Kuo, Phys. Rev. B **66**, 085121 (2002).
[31] A. Abragam, *Principles of Nuclear Magnetism* (Oxford University Press, New York, 1982).
[32] J. J. Spokas and C. P. Slichter, Phys. Rev. **113**, 1318 (1959); A. G. Anderson and A. C. Redfield, *ibid.* **116**, 583 (1959).